LAWRENCE
LIVERMORE
NATIONAL
LABORATORY

Bremsstrahlung and K(alpha) fluorescence measurements for inferring conversion efficiencies into fast ignition relevant hot electrons

C. D. Chen, P. K. Patel, D. S. Hey, A. J. Mackinnon, M. H. Key, K. U. Akli, T. Bartal, F. N. Beg, S. Chawla, H. Chen, R. R. Freeman, D. P. Higginson, A. Link, T. Y. Ma, A. G. MacPhee, R. B. Stephens, L. D. Van Woerkom, B. Westover, M. Porkolab

Disclaimer

This document was prepared as an account of work sponsored by an agency of the United States government. Neither the United States government nor Lawrence Livermore National Security, LLC, nor any of their employees makes any warranty, expressed or implied, or assumes any legal liability or responsibility for the accuracy, completeness, or usefulness of any information, apparatus, product, or process disclosed, or represents that its use would not infringe privately owned rights. Reference herein to any specific commercial product, process, or service by trade name, trademark, manufacturer, or otherwise does not necessarily constitute or imply its endorsement, recommendation, or favoring by the United States government or Lawrence Livermore National Security, LLC. The views and opinions of authors expressed herein do not necessarily state or reflect those of the United States government or Lawrence Livermore National Security, LLC, and shall not be used for advertising or product endorsement purposes.

Bremsstrahlung and Kα fluorescence measurements for inferring conversion efficiencies into fast ignition relevant hot electrons

C.D. Chen[1], P.K. Patel[2], D.S. Hey[2], A.J. Mackinnon[2], M.H. Key[2], K.U. Akli[5], T. Bartal[3], F.N. Beg[3], S. Chawla[3], H. Chen[2], R. R. Freeman[4], D.P. Higginson[3], A. Link[4], T.Y. Ma[2,3], A.G. MacPhee[2], R.B. Stephens[5], L.D. Van Woerkom[4], B. Westover[3], M. Porkolab[1]

[1]*Plasma Science Fusion Center, Massachusetts Institute of Technology, Cambridge, MA 02139*

[2]*Lawrence Livermore National Laboratory, Livermore, CA 94550*

[3]*Department of Mechanical and Aerospace Engineering, University of California-San Diego, La Jolla, CA 92093*

[4]*College of Mathematical and Physical Sciences, The Ohio State University, Columbus, OH 43210*

[5]*General Atomics, San Diego, CA 92121*

ABSTRACT

The Bremsstrahlung and K-shell emission from 1 mm x 1 mm x 1 mm planar targets irradiated by a short-pulse 3×10^{18}-8×10^{19} W/cm^2 laser were measured. The Bremsstrahlung was measured using a filter stack spectrometer with spectral discrimination up to 500 keV. K-shell emission was measured using a single photon counting charge coupled device (CCD). From Monte Carlo modeling of the target emission, conversion efficiencies into 1-3 MeV electrons of 3-12%, representing 20-40% total conversion efficiencies were inferred for intensities up to 8×10^{19} W/cm^2. Comparisons to scaling laws using synthetic energy spectra generated from the intensity distribution of the focal spot imply slope temperatures less than the ponderomotive potential of the laser. Resistive transport effects may result in potentials of a few hundred kV in the first few tens of microns in the target. This would lead to higher total conversion efficiencies than inferred from Monte Carlo modeling but lower conversion efficiencies into 1-3 MeV electrons.

I. Introduction

The Fast Ignition[1] concept promises higher gains, lower sensitivity to hydrodynamic instabilities, and reduced driver energy when compared to conventional Inertial Confinement Fusion (ICF). This is achieved using a short-pulse laser to ignite a hot spot in a pre-compressed, 300 g/cc fusion capsule. The laser interacts with the plasma near the critical density surface, generating hot electrons that propagate into the core to heat the hot spot. In cone-guided fast ignition[2,3,4], a high Z cone keeps a channel open in the blowoff plasma, reducing the distance the electrons have to travel to reach the core. The success of Fast Ignition is primarily dependent on the coupling of the short-pulse laser energy to the hot spot. This can be broken down into 3 components: the coupling of the laser into relativistic electrons ($\eta_{L \rightarrow e^-}$), the transport efficiency of the electrons to the core, which depends on the divergence angle and collimation effects (η_{trans}), and the deposition of the electron energy in the hot spot, which is a function of the electron energy spectrum ($\eta_{deposition}$). Simulations[5] have found that to achieve ignition at 300 g/cc, 18 kJ of energy must be deposited in a 40 μm diameter hot spot in 20 ps, requiring laser intensities of 2-3x10^{20} W/cm^2. For a 40 μm diameter hot spot, electrons of 1-3 MeV have the ideal range to couple efficiently, making the conversion efficiency to 1-3 MeV electrons a critical parameter for fast ignition. For intensities of 2-3x10^{20} W/cm^2, scaling of the electron energy with the ponderomotive potential of the laser[6] gives temperatures of 6-8 MeV, reducing the deposition efficiency and driving up the driver requirements. Recent modeling suggests, however, that the slope temperature may be colder than ponderomotive scaling due to steepening of the density gradient[7,8,9].

Previous measurements of the electron spectrum have relied on techniques such as vacuum electron spectrometers[10,11], nuclear activation[12], Bremsstrahlung spectrometers[13], buried fluorescent foils[14], and proton emission[15]. Measurements using electron spectrometers and nuclear activation have found that the electron slope temperature scales with the laser intensity in proportion to $(I\lambda^2)^{1/2}$ and is close to the ponderomotive potential of the laser. The energies of escaping electrons are however modified by megavolt potentials and significant modeling is required to accurately infer the source

2

spectrum at 1-3 MeV energies of most interest to fast ignition. Nuclear activation is sensitive to photons above 8 MeV and provide limited information about 1-3 MeV electrons. Other measurements using Bremsstrahlung and rear surface proton emission have found a $(I\lambda^2)^{1/3}$ scaling, usually referred to as Beg scaling[15].

Conversion efficiencies have been determined by measuring and modeling the Kα yield in very thin foils with strong refluxing. Myatt and Theobald[16] and Nilson[17] found coupling efficiencies of 20%±10%, independent of the laser intensity for I=10^{17} to 10^{20} W/cm^2 using a hybrid particle in cell model. This model did not include energy transfer to fast ions, making these measurements lower bounds on the conversion efficiency. Yasuike[14] used the fluorescence yields from buried layer Kα emitters in thick non-refluxing foils to infer both the slope temperature and conversion efficiency, estimating conversion efficiencies scaling from 10-50% for I=10^{18} to 10^{20} W/cm^2 from Monte Carlo modeling. However, the slope temperature inferred using MC modeling is sensitive to collective electric and magnetic field effects which were not included in the analysis. Davies has shown that neglect of the Ohmic potential results in an underestimate of the conversion efficiency[18].

In this paper we describe measurements of the number of 1-3 MeV electrons using absolute Bremsstrahlung and K-shell fluorescence emission from planar foil targets irradiated by a short-pulse laser. From Monte Carlo transport modeling, the laser conversion efficiency into fast ignition relevant 1-3 MeV electrons is inferred by fitting both the Bremsstrahlung measurements and the fluorescence yield. The sensitivity of the inferred conversion efficiency to the details of the method of analysis parameters is also discussed. The results are compared to scaling laws and modeling estimates commonly used in simulations of fast ignition.

This paper starts with an overview of the experiment and Bremsstrahlung and K-shell diagnostics. It then describes the Monte Carlo simulation of the target and techniques for unfolding the electron spectrum from the simulation. This is followed by comparison of the data to different scaling

laws and summaries of the inferred conversion efficiencies. The paper concludes with a discussion on the role of the assumed electron cone angles and resistive transport effects on the deduction of the conversion efficiencies.

II. Experiment Overview

Experiments were performed on the TITAN laser at Lawrence Livermore National Laboratory[19]. TITAN is a 1.06 µm laser with a maximum energy of 150 J at 0.7 ps pulse length. Focusing is with an f/3 off-axis parabola. The focal spot at target chamber center was imaged at low power with a 16-bit charge-coupled device (CCD) camera which shows a full width at half maximum (FWHM) of 7 µm and ~15% of the laser energy within the FWHM. The pre-pulse was measured on each shot with a water cell protected fast diode and the pre-formed plasma was diagnosed with a $2\omega_0$ interferometer. Pre-pulse levels for the data shown here ranged from 5-80 mJ in a 3 ns pedestal before the main pulse with a 1-30 mJ parasitic short pulse 1.4 ns ahead of the main pulse[20]. From hydrodynamic modeling of the pre-pulse, pre-formed plasma scale lengths are estimated at up to 10 µm for the critical surface and 50 µm for $1/10^{th}$ critical. The pulse length was measured at 0.7±0.3 ps using a 2nd order autocorrelator.

The targets consisted of 1 mm x 1mm sandwich targets, layered with 10 µm Al at the interaction surface, 25 µm Cu for a fluor, and a 1 mm Al layer to range out the electrons and prevent multiple passes through the Cu (refluxing). They were irradiated at 16° horizontal off normal s-polarization with 5 J to 150 J of laser energy for intensities averaged over the FWHM region (containing 15% of the laser energy) of $3x10^{18}$ W/cm^2 to $8x10^{19}$ W/cm^2. Two filter stack Bremsstrahlung spectrometers[21] measured the x-ray emission at rear target normal and at 23° horizontal to rear target normal, about 80 cm from the target. A Spectral Instruments SI-800 CCD operating in single hit mode[22] was used to measure the K-shell emission from the buried Cu layer at 24° horizontal to the front target normal. A schematic of the setup is shown in Figure 1.

III. Bremsstrahlung Spectrometer Description and Calibration

The Bremsstrahlung spectrometer consists of a stack of 13 filters from 100 µm Al to 4 mm Pb alternating with Image Plate (IP) dosimeters. It is able to differentiate photons up to 500 keV. A magnet was used to eliminate electron contamination (< 100 MeV) and a 5" Pb collimator with a ½" diameter hole limited the field of view to 5 cm at the target plane to minimize fluorescence from other diagnostics and the chamber walls. The filter stack is also enclosed within a 6 mm thick interlocking Delrin cartridge loaded into a 1.8 cm Pb housing. This spectrometer is described in greater detail elsewhere[21].

The spectrometer was calibrated at the High Energy X-ray (HEX) Laboratory (NSTec, Livermore, CA). The HEX facility produces K-shell line energies by exposing fluorescent foils to a 160 kV x-ray source. The spectrometer was calibrated with 11 K-shell sources from Zr to Pb, representing line energies of 16 (Zr kα) to 85 (Pb kβ) keV. The photon flux was measured using a Canberra high-purity germanium detector previously calibrated with NIST-traceable sources. Additionally, the spectrometer was calibrated with a Cs-137 source (662 keV photon) at the Radiation Calorimetry Laboratory (RCL) at Lawrence Livermore National Laboratory to provide a single high energy calibration point. The dosimeter signals were compared to 1-D Monte Carlo simulations of the filter stack calculated using the Monte Carlo code Integrated Tiger Series 3.0 (ITS 3.0)[23]. The simulations were used to generate a Spectrometer Response Matrix (SRM), representing the dose on each image plate for incident photons from 1 keV to 100 MeV energies. Fig. 2 shows the calibration for 4 of these data points, at 22, 57, 75, and 662 keV. The data points are the image plate readouts and the solid lines represent the predictions of the Monte Carlo model, normalized to the data. The responses are scaled to show them on the same plot. The calibration data show that the Monte Carlo model is a good representation of the response function. Additionally, the absolute calibration factor determined from scaling the model to the data

was found to be consistent for each of the exposures. This calibration factor scales the readout from scanner units to an absolute energy deposition in the image plates.

IV. Experimental Data

The data from the Bremsstrahlung spectrometer are scanned images of the 13 IPs with a projection of the collimator hole on each one. Figure 3a shows a sample of six of these channels. For each of the IP channels the mean is taken as the signal level for that channel. The error in the signal level for each channel is quantified as the quadrature addition of 3 different parameters: the standard deviation in each channel, the gradient across the projection, and a 3% response variability in the image plate scanner. The standard deviation about the mean in each channel is related to the uniformity of the dose and thus the statistics of the deposition. The gradient is taken as the difference in the mean across different parts of the image (away from the boundary) and is a measure of 3-D effects in the spectrometer modeling. The 3% image plate response variability is seen in shot to shot calibration exposures. Figure 3b shows sample data for a 18 J shot and a 121 J shot. The cutoff energy and the slope of the dosimeter signals clearly indicate a trend toward an increasing Bremsstrahlung slope temperature with increasing laser intensity. The signals and errors from each of the spectrometer channels, together with the Monte Carlo modeled SRM constitute a "few channel spectrometer" problem. The unfolding of the photon spectrum is described later in this paper.

The Kα data from the Single Hit Spectrometer are shown in Figure 4. The CCD image was processed using a "single event" algorithm where only photons which deposit all of their energy in a single pixel are counted. The yield is calculated by factoring in the detection efficiency of the chip (as a function of chip crowding), the solid angle, and filter transmissions. The calculated yields have an error bar of 20% based on the statistics of the signal and on the error in the detection efficiency as calibrated

by Maddox et al.[22] These yields are not corrected for the opacity of the target and are considered the

number of photons escaping from the target at the view angle of the spectrometer. The blue diamonds

show the yield in units of photons/SR and the red square represent the same data normalized to the

laser energy. The normalized yields are flat with the laser energy, which shows that the Kα yield scales

linearly with the laser energy. The normalized yields are plotted on a linear axis to highlight the shot to

shot variation, which is up to 30%.

V. Target Simulation

The Bremsstrahlung and K-shell emission from the electron-target interaction was modeled in 3-

D using an ITS simulation. 81 narrow spectral bins of electrons logarithmically spaced from 10 keV to

100 MeV are injected at the target surface in a 30 μm spot. The electron beam directionality and

electron cone angle are variable parameters in the simulation. The beam direction is varied between 0°

and 16°, consistent with experiments by Santala et al.[24] which found that the beam direction varied

between target normal to along the laser axis depending on the preformed plasma scale length. The

electron cone angle was assumed to have a distribution based on the classical electron ejection angle of

electrons in a laser field[25] ($\theta_{half} = \tan^{-1}\left[\left(\dfrac{2}{\gamma-1}\right)^{1/2}\right]$). This assumption follows work by Stephens[26],

where images from buried fluorescent foils showed a broad 70-100 μm Kα spot up to 100 μm depth,

followed by a 40° (full) divergence angle. From Monte Carlo simulations the assumption of the classical

ejection angle was consistent with the measured cone angle distribution. For reference a constant 40°

full cone angle response was also simulated. Recent hybrid-PIC simulations by Honrubia[27] have found

that initial electron cone angles consistent with the classical ejection angle reproduced mean divergence

angles of 30-40° seen in experiments due to magnetic collimation effects. The net propagation angle in

7

Monte Carlo simulations is not reduced by collimation so the initial cone angle is expected to be bounded by these two parameter choices.

For each combination of simulation parameters and spectrometer locations, a Target Response Matrix(TRM) is generated, representing the Bremsstrahlung emission from the target for the injected electron energies. The Bremsstrahlung spectrum is averaged over 5° polar angular bins, and 20° azimuthal bins for the off-axis directionality. The Kα emission detected by the Single Hit Spectrometer is also calculated, generating a Kα Response Matrix (KαRM) for each parameter combination.

From this model, the Bremsstrahlung emission for various electron energies is plotted in Figure 5 up to the 500 keV differential photon sensitivity of the spectrometer. There is a clear distinction between 200 keV, 1 MeV, and 2 MeV. Between 2 and 3 MeV the photon spectrum starts to look similar in the energy range of the spectrometer. The 500 keV differential photon sensitivity of the spectrometer thus maps to a 2-3 MeV differential electron sensitivity.

The SRM and TRM are multiplied together for the overall response matrix, representing the response of the dosimeter layers to electrons injected into the target. This constitutes a classic few channel spectrometer problem, and the electron spectra can be unfolded using a number of techniques, such as fitting test distributions, maximum entropy methods, or singular value decomposition. Here, one and two temperature test distributions seen in previous experimental and computational work[13,15,28] are used to determine the band of spectra consistent with the data.

VI. Electron Spectrum Unfolding and Comparisons to Scaling Laws

A. One Temperature Parameterizations

Previous comparisons to intensity scaling laws[10,12,13] have typically compared a single electron slope temperature (T_{hot}) to a single intensity parameter used to characterize the laser. If this is done with the data here, a single electron slope temperature provides a good fit to the Bremsstrahlung data.

The fit is characterized by the weighted, reduced χ^2 fitting parameter, where $\chi^2<1$ means on average the predictions fit the measured data within their error bars. The single slope temperature distributions fit the data within 1 χ^2. The beam directionality is set by the requirement that the electron slope temperature must be simultaneously consistent for both spectrometers. If the assumed directionality is along the target normal (TN), the spectrometer along TN will infer a lower temperature than the spectrometer along the laser axis (LA). For a given measured spectrum, the LA spectrometer assumes the actual spectrum is harder since it is not measuring the center of the beam. If the beam directionality is taken along the laser axis, the TN spectrometer likewise assumes a harder spectrum. The beam direction is taken as the angle at which the predicted temperatures are equal. The best fit temperature is thus taken as the temperature that is simultaneously consistent with the measurements from both spectrometers. This works better for higher intensities since the electron cone angle is more directional. For low intensities and consequently lower energy electrons, the assumed cone angle is almost 2π and the beam directionality does not matter. The calculated beam directionality varied from 6 to 16 degrees.

Using the FWHM-averaged peak intensity as previously discussed, the slope temperatures are consistent with Beg scaling ($T_{hot}=215 \, (I_{18}\lambda^2)^{1/3}$ keV) up to $2\mathrm{x}10^{19}$ W/cm^2, and 20-40% higher than Beg scaling for intensities up to $8\mathrm{x}10^{19}$ W/cm^2. For the 121 J shot shown in Figure 3b, the single-temperature fit has a T_{hot} of 1.3 ± 0.1 MeV. Beg scaling predicts a 0.9 ± 0.1 MeV T_{hot} (error bar from the pulselength uncertainty), about 40% lower ($\chi^2=10$). Ponderomotive scaling predicts 3.3 MeV, significantly hotter ($\chi^2 \approx 70$) than the single temperature fit.

This seems to suggest that Beg scaling provides a better fit to the data than ponderomotive scaling. However, this analysis is misleading for two reasons. First, the electron distributions that fit the data are not unique. Parameterization with two temperature components show that different spectra consistent with the data can be drastically different, as will be discussed shortly. Second, comparisons

9

to scaling laws using a single intensity parameter are simplistic, and do not properly account for the intensity distribution. The ponderomotive potential is a local effect, and proper estimates of the electron spectrum must account for the focal spot intensity distribution rather than just a single peak intensity. Empirical scalings like the Beg scaling law correlate the slope temperature with a defined intensity; as long as a consistent intensity definition is used (which is not always the case) this should more consistently predict the slope temperature. However, it is not clear that the intensity scaling law should necessarily translate to other laser systems where the focal spot profile may be very different. Scaling law comparisons using the focal spot intensity distribution will be discussed later in this section.

B. Two Temperature Parameterizations

The spectral space of the electron distributions can be expanded by parameterizing the distribution using hot and cold temperatures and a ratio between the two components, taking the form $f(E) \propto R\,\varphi(E\,|\,T_c) + \varphi(E\,|\,T_h)$, where T_c and T_h are varied from 10 keV to 10 MeV, R from 0.1 to 1000, and φ is a normalized Boltzmann or 1-D relativistic Maxwellian distribution. The target response matrix with a beam directionality selected from the 1-T fits is used. The matrix response model simplifies testing of the entire parameter space. The fitting parameter is calculated for 16 million distributions per shot, providing highly resolved variances of the distribution. The electron distributions that simultaneously fit both of the spectrometers within 1 χ^2 are selected as valid fits.

Figure 6a shows a sample subset of allowed distributions for a 121 J shot, represented by the color lines, along with the envelope of fits, represented by the solid black lines. A broad range of electron distributions are consistent with the data, with almost an order of magnitude difference in the number of electrons at any given energy. The straight brown line in 6a represents a single temperature distribution with a 1.3 MeV slope temperature. The other sample distributions show, however, that this single temperature is not unique and depends on the energy range in which the slope is measured. The

solid black lines define the envelope in which the 2-T solutions fall. The envelope itself is not a solution. The envelope serves to bound the spectral space for this shot.

All of these electron distributions generate similar photon spectra up to the differential sensitivity limit of the spectrometer. The solid black lines in Figure 6b represent the envelope of Bremsstrahlung distributions generated by the different electron spectra. This envelope is significantly narrower; similar Bremsstrahlung spectra can be generated with larger numbers of colder electrons or smaller numbers of hotter electrons. Above 500 keV the spectrometer has no differential sensitivity, but the Bremsstrahlung spectrum is restricted by the assumption of an exponentially falling electron distribution (in the 2-T parameterization).

The band of unfolded electron spectra was reduced by using the Cu Kα emission from the fluorescence layer as an additional constraint. For this shot the measured Kα yield was $5.3 \times 10^{11} \pm 20\%$ photons/SR. This yield is not corrected for the target opacity since the opacity is already factored into the KαRM through the Monte Carlo simulation. The Kα signal effectively acts as a counter of electrons above 50 keV; these have sufficient energy to reach the copper layer and efficiently stimulate fluorescence. With the Kα constraint, the range of possible electron distributions is further reduced in the lower energy part of the spectrum, as shown in Figure 6c. The photon spectrum is only mildly affected, as seen in the solid red lines Figure 6b.

C.   Scaling Law Comparisons using Synthetic Electron Distributions

A better comparison to analytic scaling laws can be done by generating a synthetic spectrum from the vacuum focal spot intensity distribution. Any modifications due to self focusing in the preformed plasma are not included here. The intensity distribution is binned in time and space using the focal spot image and a 0.7 ps Gaussian temporal profile as measured from the autocorrelator trace. A conversion efficiency and electron energy spectrum is then assigned to each intensity element in

space and time using an exponential distribution with a slope temperature from the scaling law and a given conversion efficiency model. Here the flat coupling inferred by Myatt and Nilson is used, with the coupling efficiency scaled to the measured data (alternatively Yasuike's 10-50% coupling efficiency would make the hot tail of the electron distribution slightly hotter and would increase the discrepancy shown later here between the measured data and the ponderomotive model for temperature). The synthetic distribution is then generated by integrating these electron distributions in space and time. This spectrum does not have a single temperature, and the slope temperature is higher when measured at higher energies.

Synthetic electron distributions were generated for three intensity scaling models: ponderomotive scaling, ponderomotive scaling reduced by a 75% scale factor, and the parameterization of density gradient steepening by Chrisman, Sentoku, and Kemp[8].

Wilks' original 1992 PIC simulations[6] of ponderomotive scaling show a +/-25% difference in electron temperatures about the ponderomotive potential for p and s-polarized light, respectively. A synthetic spectrum can then be generated by reducing the ponderomotive temperature by a scale factor, i.e. $T_h = f\ T_{POND}$. Since this experiment was performed with a near-normal, s-polarized laser, a synthetic spectrum using f=75% is thus considered within the "error bar" of ponderomotive scaling.

Recent simulations by Chrisman and Sentoku[8], and Kemp[7] have shown a reduction in the slope temperature due to light pressure induced steepening of the density gradient. This arises from shortening of the jxB acceleration distance by a factor $\sqrt{\frac{\gamma n_c}{n_s}}$, where n_s is the density of the steepened shelf. From 2-D PIC simulations, the energy spectrum was parameterized by splitting the hot electrons into two components, one with a slope temperature equal to the ponderomotive potential and the other reduced by the factor $\sqrt{\frac{\gamma n_c}{n_s}}$, with each component containing half of the electron energy.

The synthetic spectra generated from these three models are compared to the experimental data in Figure 7. The main figure shows the comparison to the Bremsstrahlung data, while the inset shows the comparison to the measured Kα signal. The synthetic ponderomotive spectrum is still slightly hotter than the data (χ^2=8) but the fit is significantly better than the 3.3 MeV single temperature ponderomotive distribution. The Chrisman parameterization and the 75% ponderomotive model fit the measured data within the error bars. The Bremsstrahlung spectrum predicted by the Chrisman and 75% ponderomotive models is almost exactly the same up to the differential sensitivity limit of the spectrometer. The Kα signal is shown in the insert by the horizontal orange line, with its associated 20% error bar. The ponderomotive spectrum and the 75% ponderomotive spectrum underpredict the Kα signal by about a factor of two. The Chrisman parameterization is consistent with the measured Kα signal within its error bars.

The Chrisman parameterization provides the best fit to both the Bremsstrahlung and Kα data in this Monte Carlo model. Resistive transport effects neglected in the Monte Carlo simulations are a potential source of uncertainty, and will be assessed later in this paper.

VII. Conversion Efficiency Scalings with Intensity

The total conversion efficiency ($\eta_{L\rightarrow e^-}$) and the conversion efficiency into 1-3 MeV ($\eta_{L\rightarrow 1\text{-}3\,\text{MeV}\,e^-}$) electrons is calculated for each of the 2-T distributions previously described. Figure 8a shows the scaling of $\eta_{L\rightarrow 1\text{-}3\,\text{MeV}\,e^-}$ with laser intensity. The solid gray bars represent the predicted conversion efficiencies for the spectra that fit the Bremsstrahlung data with 1 χ^2; the orange bars also fit the Kα constraint within its 20% error bars. $\eta_{L\rightarrow 1\text{-}3\,\text{MeV}\,e^-}$ peaks around 2×10^{19} W/cm^2 and then falls off. The conversion efficiency into 1-3 MeV electrons is banded between 3-12%. For reference, the black line represents the conversion efficiency into 1-3 MeV electrons assuming a Boltzmann distribution with ponderomotive scaling using the FWHM average intensity and a 22% conversion efficiency. With standard

ponderomotive scaling, $\eta_{L\to1\text{-}3\,MeV\,e\text{-}}$ peaks at too low an intensity compared to the data, suggesting that the calculated spectrum needs to take into account both the focal spot distribution and a possible reduction in the temperature. The total conversion efficiencies are shown in Figure 8b. The total conversion efficiencies are banded between 20-40%. This is slightly higher than the 10-30% minimum conversion efficiencies measured by Nilson et al., which is probably due to their neglect of energy transfer to fast ions.

The conversion efficiencies predicted from the synthetic spectra from the various scaling models are shown in Table 1. For the 121 J shot, the electron distributions consistent with both the Bremsstrahlung spectrum and the Kα constraint bound $\eta_{L\to e\text{-}}$ between 20-31% and $\eta_{L\to1\text{-}3\,MeV\,e\text{-}}$ between 2.5-8%. The synthetic ponderomotive spectrum results in a total conversion efficiency lower than these bounds (while the distribution shape is given by the models, the absolute conversion efficiency is scaled to the data). The Chrisman conversion efficiencies are calculated to be $\eta_{L\to e\text{-}}$=25% and $\eta_{L\to1\text{-}3\,MeV\,e\text{-}}$=4.6%. The higher conversion efficiency is due to the larger number of prescribed colder electrons which contribute to the energy of the spectrum but do not produce significant levels of Bremsstrahlung. At these intensities, the Chrisman parameterization has nearly the same energy fraction of 1 to 3 MeV electrons as the ponderomotive scaling. At higher intensities required for ignition more of the low energy component of the spectrum would fall in the energy range of interest so the useful fraction would increase.

The 75% ponderomotive spectrum results in more energy going into 1-3 MeV electrons by reducing the temperature of the higher energy tail. This model does not prescribe a large bulk of low energy electrons that inflate the total conversion efficiency of the Chrisman model.

Model	$\eta_{L\to e\text{-}}$	$\eta_{L\to1\text{-}3\,MeV\,e\text{-}}$
2-T parameterization	20-31%	2.5-7.7%
Ponderomotive	16%	5.3%
75% Ponderomotive	20%	6.9%

Chrisman	25%	4.6%

Table 1. Conversion efficiencies for the synthetic electron spectra for the 121 J shot.

VIII. Discussion and Systematic Uncertainties

The requirements for ignition have been the subject of several modeling studies[5,27,29]. Atzeni[5]

assumes for example a 25% total conversion efficiency and a hot electron temperature consistent with

ponderomotive scaling, resulting in electrons with too large a range for optimal coupling to the hot spot.

The total conversion efficiency measured here is consistent with that assumption, with electron

temperatures giving a more optimal range, suggesting somewhat more favorable conditions. The cone

angle assumed here, however, ranges from 90-60° for 1-3 MeV electrons. This would result in a

transport cone angle worse than usually assumed in modeling of ignition. Magnetic focusing of the

electron beam at ignition scale conditions mitigates the effect of divergence of the source electrons and

is a subject of ongoing study[30,31].

There are two primary sources of error that systematically bias this analysis, the assumption of

the electron cone angle and the neglect of resistive transport effects.   In contrast to the classical

ejection angle assumption, if all the electrons are launched into a 40° cone angle whether by magnetic

collimation or otherwise, the calculated conversion efficiencies for the 121 J shot would be $\eta_{L \to e_-}$=16-

22% and $\eta_{L \to 1\text{-}3 \text{ MeV } e_-}$=1.6-5.4% (with the K$\alpha$ constraint). The full conversion efficiency is 25% lower and

the conversion efficiency into 1-3 MeV electrons is reduced by 30-40%. The angular distribution of the

electrons is the main uncertainty in unfolding the electron spectrum from the Bremsstrahlung

measurements. A full spectral and angular measurement, similar to work by Schwoerer[32], or imaging of

multiple fluorescent layers buried in the target could help provide additional constraints on the angular

distribution.

The other source of error is the neglect of collective electric and magnetic effects in the

transport model. While collective fields are not present in a basic Monte Carlo model, the impact can be

estimated using a Bell-like[33] model where an Ohmic potential drives a return current of thermal electrons. The magnitude of the potential in these experiments is estimated using an initial electron spectrum from Chrisman parameterization using the focal spot intensity distribution and a 25% conversion efficiency, as described above. The electrons are binned into energy groups and are launched from a 30 μm diameter spot into a cone angle given by the classical ejection angle. The electric field is given by

$$E(z) = \eta(z)\, j(z) = \eta(z) \sum_i \frac{N_i e}{\pi \tau} \frac{1}{\left(r_0 + z \tan \theta_i\right)^2} H\!\left(R_i - z\right)$$

where η is the resistivity of the material, N_i is the number of electrons in each energy group, r_0 the initial spot size, θ_i the divergence angle of each energy group, H the Heaviside step function, and R_i the range of the electrons in each energy group.

The electric field is calculated as a function of depth with a cutoff at the electron range. The electrons lose energy through collisional, radiative, and resistive effects. The collisional and radiative losses are taken from tabulated values for cold matter[34]. Scattering is included in a rough way by taking the electron path length as two times greater than the linear penetration depth, which has been shown for energies from 10 keV to several MeV[35,36]. The electron range is thus approximated by integrating the energy loss against the potential into the target along with twice the collisional and radiative losses. The electric field is calculated and summed for all energy groups and integrated for a potential across the target. This procedure is then iterated to converge upon a self-consistent solution of the potential and electron penetration depth.

Using this formulation, the potential across the target is calculated at 700 kV if a peak aluminum resistivity of about 1.5×10^{-6} Ω-m is used for the entire bulk, assuming that most of the interaction occurs at temperatures between 10 eV and 100 eV for which the resistivity of Al is close to the peak value. Half of the potential is in the first 10 μm, and ¾ is in the first 30 μm, before the electrons have had a chance

to spread. The calculated potential is temperature dependent and may be lower depending on the

actual temperature distribution in the target. 3-D currents may also serve to partially lower the front

surface charge buildup and thus reduce the potential felt by the hot electrons. Regardless, given the

electron currents in these experiments, the potential is likely to be at least a couple hundred kV.

Neglecting this potential in a Monte Carlo analysis may influence the interpretation of the

conversion efficiencies. Since the majority of the potential is in the first few tens of microns and the

Bremsstrahlung is produced throughout the bulk, all of the electrons producing Bremsstrahlung in the

target pass through this potential. The electron spectrum is essentially downshifted by this potential

before it produces Bremsstrahlung. The electron spectrum inferred from the measured Bremsstrahlung

emission just needs to be upshifted by the potential. If the mean energy is taken as the 1.3 MeV single

temperature fit, a shift of a couple hundred kV would slightly perturb the inferred conversion

efficiencies. The synthetic ponderomotive spectrum discussed in section VIc is also within range of this

potential Ohmic correction. Transport simulations similar to those by Davies[18] and Honrubia[27] are

necessary to quantify the shift in the spectrum. The Kα emission is strongly influenced by the Ohmic

potentials, as previously discussed by Davies. With the Monte Carlo analysis, the fluor acts as a counter

of electrons above 50 keV. If there is a potential of a couple hundred kV in the first ten microns before

the fluor, the energy at which this counter acts is upshifted to a few hundred keV. This could

significantly reduce the number of Kα photons predicted by the Chrisman parameterization, and may

result in better agreement of that model with the data.

The impact of the Ohmic potentials on the Kα constraint is mixed. Some of the electron spectra

in Figure 6a with larger numbers of electrons in the hundred of keV range produce too much Kα in the

Monte Carlo model to be consistent with measured Kα emission. With an Ohmic model, these

distributions would be consistent with the data. This would result in an upward revision of the total

conversion efficiency since there would be larger numbers of low energy electrons. The conversion

efficiency into 1-3 MeV electrons is likely to drop since fewer high energy electrons would be needed to produce the measured Bremsstrahlung emission. In Figure 8b, $\eta_{L \to e^-}$ consistent with the Kα is at the lower range of the band consistent with the Bremsstrahlung. In Figure 8a, $\eta_{L \to 1\text{-}3 \text{ MeV } e^-}$ consistent with the Kα is at the upper range of the band consistent with the Bremsstrahlung. Both of these conversion efficiencies are likely to shift towards the median when resistive effects are accounted for.

Magnetic fields may enhance the energy loss near the front surface of the target and reduce the penetration lengths by increasing the curvature of the electron path[18]. The impact of magnetic fields on the conversion efficiency would thus be analogous to that of the Ohmic potential.

IX. Conclusions

The Bremsstrahlung spectrum and Kα emission of a fluorescent layer have been measured in non-refluxing targets. Through Monte Carlo modeling, conversion efficiencies into 1-3 MeV electrons of 3-12% have been inferred. This represents a total conversion efficiency of 20-40%. Assumptions of the angular distribution model are a major source of uncertainty in the analysis. Better comparisons to scaling laws used synthetic energy spectra generated from the intensity distribution of the foal spot. Forward calculations of the electron spectra for various intensity scaling models were compared to the Bremsstrahlung data. The forward calculations are suggestive of energy spectra with lower slope temperatures than scaling with the ponderomotive potential of the laser. Resistive effects result in potentials of a few hundred kV in the first tens of microns in the target. This may result in higher total conversion efficiencies than inferred from Monte Carlo modeling but lower conversion efficiencies into the 1-3 MeV band of primary interest to fast ignition.

X. Acknowledgements

References

1. M. Tabak, J.E. Hammer, M.E. Glinsky, W.L. Kruer, S.C. Wilks, J. Woodworth, E.M. Campbell, M. Perry, and R. J. Mason, Phys. Plasmas **1**, 1626-1634 (1994).

2. M. Tabak, J. H. Hammer, E. M. Campbell, W.L, Kruer, J. Goodworth, S.C. Wilks, and M. Perry, *Lawrence Livermore National Laboratory patent disclosure*, No. IL8826B, 1994, Lawrence Livermore National Laboratory, Livermore, CA; S. Hatchett and M. Tabak, "Cone focus geometry for Fast Ignition," presented at the 30th Annual Anomalous Absorption Conference, Ocean City, MD (April 2000); S. Hatchett, M. Herrmann, M. Tabak, R. Turner, and R. Stephens, Bull. Am. Phys. Soc. **46**, BP1.086 (2001).

3. R. Kodama, P.A. Norreys, K. Mima, A.E. Dangor, R.G. Evans, H. Fujita, Y. Kitagawa, K. Krushelnick, T. Miyakoshi, N. Miyanaga, T. Norimatsu, S.J. Rose, T. Shozaki, K. Shigemori, A. Sunahara, M. Tampo, K.A. Tanaka, Y. Toyama, T. Yamanaka, and M. Zepf, Nature **412**, 798-802 (2001).

4. R. Kodama, H. Shiraga, K. Shigemori, Y. Toyama, S. Fujioka, H. Azechi, H. Fujita, H. Habara, T. Hall, Y. Izawa, T. Jitsuno, Y. Kitagawa, K.M. Krushelnick, K.L. Lancaster, K. Mima, K. Nagai, M. Nakai, H. Nishimura, T. Norimatsu, P.A. Norreys, S. Sakabe, K.A. Tanaka, A. Youssef, M. Zepf, and T. Yamanaka, Nature **418**, 933-934 (2002).

5. S. Atzeni, A. Schiavi, and C. Bellei, Phys. Plasmas **14**, 052702 (2007).

6. S.C. Wilks, W.L. Kruer, M. Tabak, and A.B. Langdon, Phys. Rev. Lett. **69**, 1383-1386 (1992).

7. A. J. Kemp, Y. Sentoku, and M. Tabak, Phys. Rev. Lett. **101**, 075004 (2008).

8. B. Chrisman, Y. Sentoku, and A. J. Kemp, Phys. Plasmas **15**, 056309 (2008).

9. M.G. Haines, M.S. Wei, F.N. Beg, and R.B. Stephens, Phys. Rev. Lett. **102**, 045008 (2009).

10. G. Malka and J.L. Miquel, Phys. Rev. Lett. **77**, 75-78 (1996).

11. K. A. Tanaka, R. Kodama, H. Fujita, M. Heya, N. Izumi, Y. Kato, Y. Kitagawa, K. Mima, N. Miyanaga, T. Norimatsu, A. Pukhov, A. Sunahara, K. Takahashi, M. Allen, H. Habara, T. Iwatani, T. Matusita, T. Miyakosi, M. Mori, H. Setoguchi, T. Sonomoto, M. Tanpo, S. Tohyama, H. Azuma, T. Kawasaki, T. Komeno, O. Maekawa, S. Matsuo, T. Shozaki, Ka Suzuki, H. Yoshida, T. Yamanaka, Y. Sentoku, F. Weber, T. W. Barbee, Jr., and L. DaSilva. Phys. Plasmas **7**, 2014-2022 (2000).

12. M.A. Stoyer, T.C. Sangster, E.A. Henry, M.D. Cable, T.E. Cowan, S.P. Hatchett, M.H. Key, M.J. Moran, D.M. Pennington, M.D. Perry, T.W. Phillips, M.S. Singh, R.A. Snavely, M. Tabak, and S.C. Wilks, Rev. Sci. Instrum. **72**, 767-772 (2001).

13. P.A. Norreys, M. Santala, E. Clark, M. Zepf, I. Watts, F.N. Beg, K. Krushelnick, M. Tatarakis, A.E. Dangor, X. Fang, P. Graham, T. McCanny, R.P. Singhal, K.W.D. Ledingham, A. Creswell, D.C.W. Sanderson, J. Magill, A. Machacek, J.S. Wark, R. Allott, B. Kennedy, and D.Neely, Phys. Plasmas **6**, 2150-2156 (1999).

14. K. Yasuike, M. H. Key, S. P. Hatchett, R. A. Snavely, and K. B. Wharton, Rev. Sci. Instrum. **72**, 1236-1240 (2001).

15. F.N. Beg, A.R. Bell, A.E. Dangor, C.N. Danson, A.P. Fews, M.E. Glinsky, B.A. Hammel, P. Lee, P.A. Norreys, and M. Tatarakis, Phys. Plasmas **4**, 447-457 (1997).

16. J. Myatt, W. Theobald, J.A. Delettrez, C. Stoeckl, M. Storm, T.C. Sangster, A.V. Maximov, and R.W. Short, Phys. Plasmas **14**, 056301 (2007).

17. P.M. Nilson, W. Theobald, J. Myatt, C. Stoeckl, M. Storm, O.V. Gotchev, J.D. Zuegel, R. Betti, D.D. Meyerhofer, and T.C. Sangster, Phys. Plasmas **15**, 056308 (2008).

18. J.R. Davies, Phys. Rev. E **65**, 026407 (2002).

19. B. C. Stuart, J. D. Bonlie, J. A. Britten, J. A. Caird, R. Cross, C. A. Ebbers, M. J. Eckart, A. C. Erlandson, W. A. Molander, A. Ng, P. K. Patel, and D. F. Price, "The Titan Laser at LLNL," in *Conference on Lasers and Electro-Optics/Quantum Electronics and Laser Science Conference and Photonic Applications Systems Technologies*, Technical Digest (CD) (Optical Society of America, 2006), paper **JTuG3**.

20. S. Le Pape, Y.Y. Tsui, A.G. Macphee, D.S. Hey, P.K. Patel, A.J. Mackinnon, M.H. Key, M. Wei, T.Y. Ma, F.N. Beg, R.B. Stephens, K.U. Akli, A. Link, L.D. Van-Woerkom, and R.R. Freeman, "Characterization of the preformed plasma for high intensity laser-plasma interaction", submitted to Optics Letters (2009).

21. C.D. Chen, J.A. King, M.H. Key, K.U. Akli, F.N. Beg, H.Chen, R.R. Freeman, A. Link, A.J. Mackinnon, A.G. MacPhee, P.K. Patel, M. Porkolab, R.B. Stephens, and L.D. Van Woerkom, Rev. Sci. Instrum. **79**, 10E305 (2008).

22. B.R. Maddox, H.S. Park, B.A. Remington, and M. McKernan, Rev. Sci. Instrum. **79**, 10E924 (2008).

23. J.A. Halbleib, R.P. Kensek, G.D. Valdez, S.M. Seltzer, and M.J. Berger, IEEE Transactions on Nuclear Science **39**, 1025-1030 (1992).

24. M.I.K. Santala, M. Zepf, I. Watts, F.N. Beg, E. Clark, M. Tatarakis, K. Krushelnick, A.E. Dangor, T. McCanny, I. Spencer, R.P. Singhal, K.W.D. Ledingham, S.C. Wilks, A.C. Machacek, J.S. Wark, R. Allott, R.J. Clarke, and P.A. Norreys, Phys. Rev. Lett. **84**, 1459-1462 (2000).

25. C.I. Moore, J.P. Knauer, and D.D. Meyerhofer, Phys. Rev. Lett. **74**, 2439-2442 (1995).

26. R.B. Stephens, R.A. Snavely, Y. Aglitskiy, F. Amiranoff, C. Andersen, D. Batani, S.D. Baton, T. Cowan, R.R. Freeman, T. Hall, S.P. Hatchett, J.M. Hill, M.H. Key, J.A. King, J.A. Koch, M. Koenig, A.J. MacKinnon, K.L. Lancaster, E. Martinolli, P. Norreys, E. Perelli-Cippo, M. Rabec Le Gloahec, C. Rousseaux, J.J. Santos, and F. Scianitti, Phys. Rev. E **69**, 066414 (2004).

27. J.J. Honrubia and J. Meyer-ter-Vehn, Plasma Physics and Controlled Fusion **51**, 014008 (2009).

28. M.H. Key, M.D. Cable, T.E. Cowan, K.G. Estabrook, B.A. Hammel, S.P. Hatchett, E.A. Henry, D.E. Hinkel, J.D. Kilkenny, J.A. Koch, W.L. Kruer, A.B. Langdon, B.F. Lasinski, R.W. Lee, B.J. MacGowan, A. MacKinnon, J.D. Moody, M.J. Moran, A.A. Offenberger, D.M. Pennington, M.D. Perry, T.J. Phillips, T.C. Sangster, M.S. Singh, M.A. Stoyer, M. Tabak, G.L. Tietbohl, M. Tsukamoto, K. Wharton, and S.C. Wilks, Phys. Plasmas **5**, 1966-1972 (1998).

29. R. Betti, A.A. Solodov, J.A. Delettrez, and C. Zhou, Phys. Plasmas **13**, 100703 (2006).

30. A.P.L. Robinson and M. Sherlock, Phys. Plasmas **14**, 083105 (2007).

31. S. Kar, A.P.L. Robinson, D.C Carroll, O. Lundh, K. Markey, P. McKenna, P. Norreys, and M. Zepf, Phys. Rev. Lett. **102**, 055001 (2009).

32. H. Schwoerer, P. Gibbon, S. Dusterer, R. Behrens, C. Ziener, C. Reich, and R. Sauerbrey, Phys. Rev. Lett. **86**, 2317-2320 (2001).

33. A.R. Bell, J.R. Davies, S. Guerin, and H. Ruhl, Plasma Physics and Controlled Fusion **39**, 653-659 (1997).

34. ICRU Technical Report 37, "Stopping powers for electrons and positrons", International Commission on Radiation Units and Measurements (1984). Oxford University Press, Journals Department, Great Clarendon Street Oxford OX2 6DP, United Kingdom.

35. B.F.J. Schonland, Proc. Roy. Soc. Lond. **108**, 187-210 (1925).

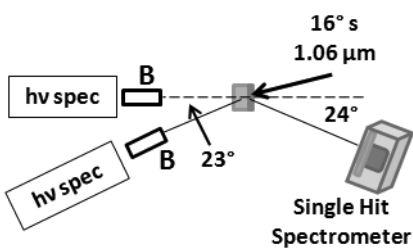36. R.W. Varder, Phil. Mag. **29**, 725 (1915).

Figures

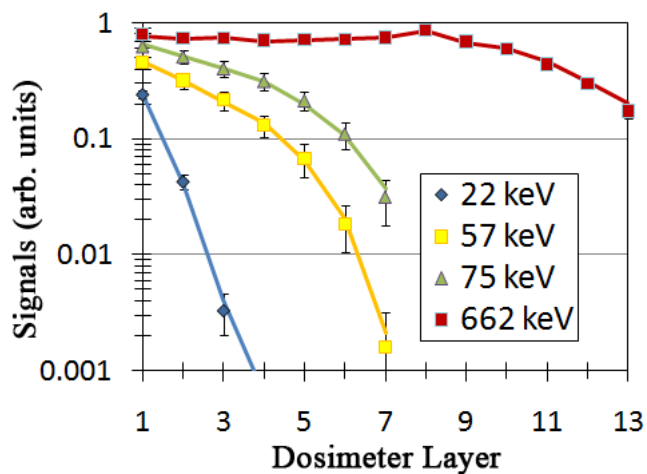Fig. 1. Schematic of the diagnostic layout

Fig. 2. (color online) The Bremsstrahlung spectrometer is calibrated from 15-85 keV and at 662 keV. The points are the measured dosimeter signals and the solid lines represent the Monte Carlo model predictions. The signals are scaled to show them on the same plot. The absolute calibration factor is consistent across the spectrum.
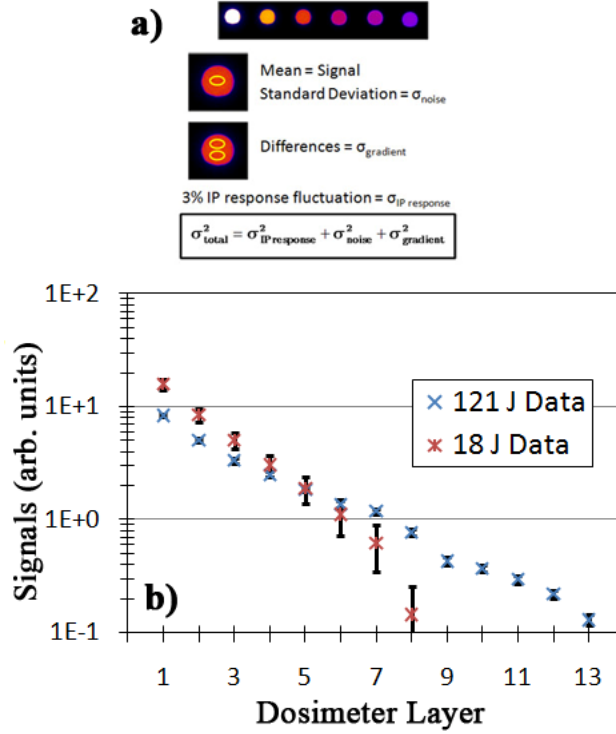
Fig. 3. (color online) Data extraction from the HXBS channels. a) The mean signal in each channel is taken as the PSL signal value. The error bar on each channel is the quadrature sum of the standard deviation in each channel, the gradient across the channel, and a 3% image plate response variation. b) Sample data for a 18 J shot and a 121 J shot. The cutoff energy and the slope of the dosimeter signals clearly indicate a trend toward an increasing Bremsstrahlung slope temperature with increasing laser intensity.
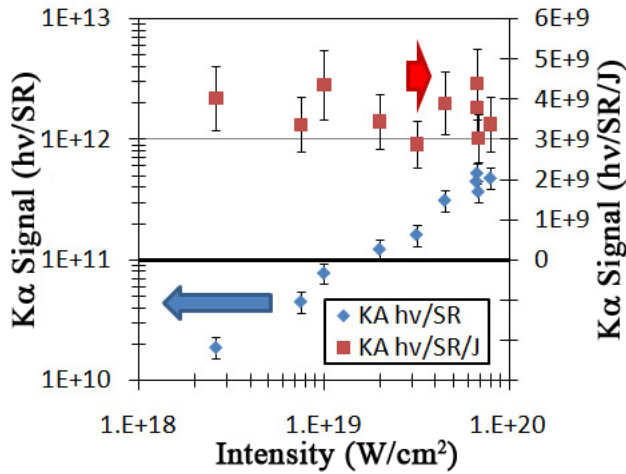
Fig. 4. (color online) A The Kα data from the Single Hit Spectrometer. These yields are not corrected for the opacity of the target and are considered the number of photons escaping from the target at the

view angle of the spectrometer. The blue diamonds show the yield in units of photons/SR and the red square represent the same data normalized to the laser energy. The Kα yield scales with the laser energy. The normalized yields are plotted on a linear axis to highlight a shot to shot variation up to 30%.
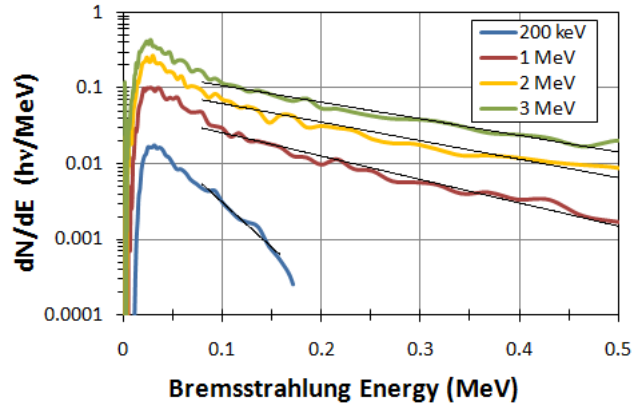

Fig. 5. (color online) The Bremsstrahlung emission for various electron energies up to the 500 keV differential sensitivity of the spectrometer. There is a distinction between 200 keV, 1 MeV, and 2 MeV. Between 2 and 3 MeV the photon spectrum converges in the energy range of the spectrometer. The 500 keV differential photon sensitivity of the spectrometer maps to a 2-3 MeV differential electron sensitivity.
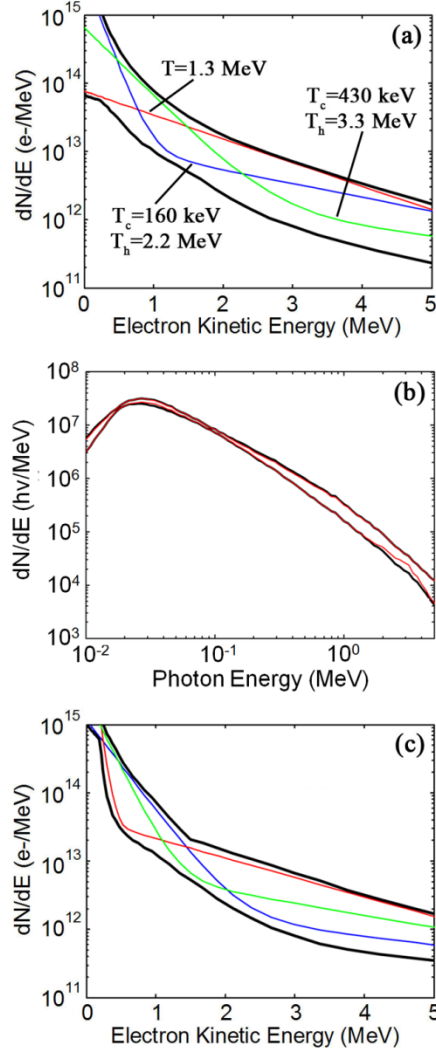
Fig. 6. (color online) (a) Various 2-T electron spectra are consistent with the spectrometer data. A sample subset of these curves are plotted, with the black lines representing the envelope of these curves. (b) The black lines represent the resultant Bremsstrahlung spectra from the electron spectra in 6a. The Bremsstrahlung is significantly more constrained, with the different electron spectra in 6a producing the same Bremsstrahlung emission. The red lines represent the Bremsstrahlung spectra from the Kα constrained electron energy spectra. (c) 2-T electron spectra consistent with both the Bremsstrahlung data and the K-shell emission. The K-shell emission acts as an electron counter that further constrains the set of possible distributions.
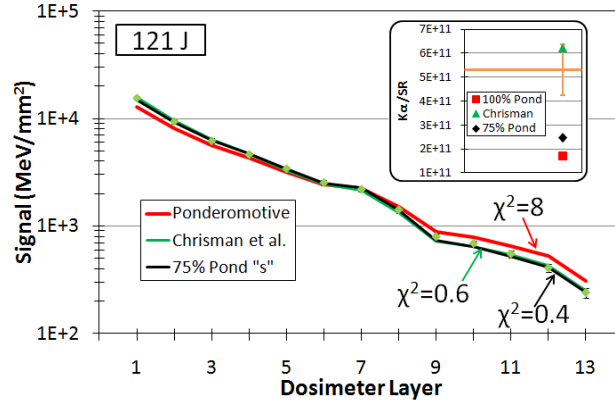
Fig. 7. (color online) The synthetic spectra derived from different T_{hot} scalings using the focal spot intensity distribution are fit to the measured Bremsstrahlung data for the 121 J shot. The synthetic ponderomotive spectrum is slightly hotter than the data. The Chrisman parameterization and 75% synthetic ponderomotive spectrum fit the Bremsstrahlung data within the error bars. The inset shows the Kα predictions of the different spectra relative to the measured data, given by the orange line and error bars. The ponderomotive and 75% ponderomotive spectra underpredict the Kα signal by a factor of two.
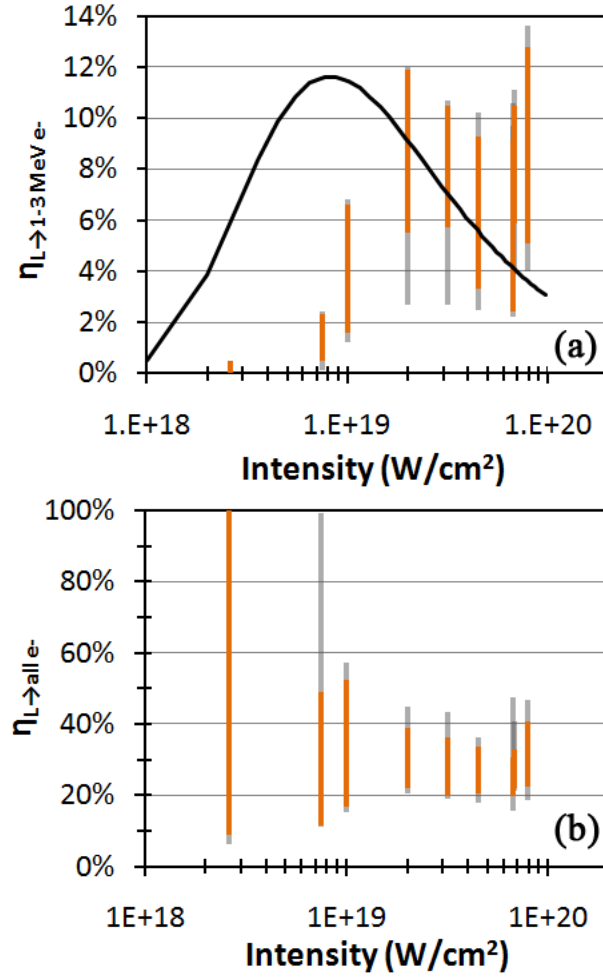
Fig. 8. (color online) (a) The conversion efficiency into 1-3 MeV electrons is plotted vs. laser intensity. The grey bars represent the predicted conversion efficiencies from the Bremsstrahlung data. The orange bars represent the conversion efficiencies also consistent with the kα measurement. Above 10^{19} W/cm^2, about 3-12% of the laser energy goes into 1-3 MeV electrons. For reference, the black line represents conversion efficiency into 1-3 MeV electrons given ponderomotive scaling with the peak intensity and a 22% total conversion efficiency. (b) Laser conversion efficiencies into all electrons range from 20-40% for intensities above 10^{19} W/cm^2.